Study of Adiabatic Obstacles on Natural Convection in a Square Cavity Using Lattice Boltzmann Method

Pawan Karki
Department of Mechanical Engineering,
National Institute of Technology Karnataka,
Surathkal, Mangalore 575025, India

Ajay Kumar Yadav
Department of Mechanical Engineering,
National Institute of Technology Karnataka,
Surathkal, Mangalore 575025, India

D. Arumuga Perumal[1]
Department of Mechanical Engineering,
National Institute of Technology Karnataka,
Surathkal, Mangalore 575025, India
e-mail: perumal@nitk.edu.in

This study involves the effect of adiabatic obstacles on two-dimensional natural convection in a square enclosure using lattice Boltzmann method (LBM). The enclosure embodies square-shaped adiabatic obstacles with one, two, and four in number. The single obstacle in cavity is centrally placed, whereas for other two configurations, a different arrangement has been made such that the core fluid zone is not hampered. The four boundaries of the cavity considered here consist of two adiabatic horizontal walls and two differentially heated vertical walls. The current study covers the range of Rayleigh number ($10^3 \leq Ra \leq 10^6$) and a fixed Prandtl number of 0.71 for all cases. The effect of size of obstacle is studied in detail for single obstacle. It is found that the average heat transfer along the hot wall increases with the increase in size of obstacle until it reaches an optimum value and then with further increase in size, the heat transfer rate deteriorates. Study is carried out to delineate the comparison between the presences of obstacle in and out of the conduction dominant zone in the cavity. The number of obstacles (two and four) outside of this core zone shows that heat transfer decreases despite the obstacle being adiabatic in nature. [DOI: 10.1115/1.4041875]

Keywords: natural convection, square cavity, lattice Boltzmann method, Rayleigh number, obstacle

1 Introduction

Lattice Boltzmann method (LBM), a mesoscopic approach, which does not trace an individual molecule but tracks particle distributions or represents collective behaviors of individual molecules is relatively a different discipline of computational fluid dynamics—absolutely one of a kind [1]. The origin of this method comes from a Boolean automata model known as the lattice gas automata (LGA) [2,3]. This method considers the movement and the collision of the particles in and around the lattice link to simulate the phenomenon of fluid flow. No sooner the LBM method was developed, this approach started gaining popularity as an alternative to well-established traditional computational fluid dynamics methods owing to its advantages over traditional approach of solving Navier–Stokes equation, ease of implementation, parallel computing, and simple handling of complex boundaries [4]. LBM has also been used to study some complex phenomena viz. turbulent flows [5], magneto-hydrodynamics [6], multicomponent flows over complex boundaries [7], and multiphase flow with phase change [8]. The success of simulating isothermal flows with this method is parallel to none. In this context, Massaoli et al. [9] were the first to develop thermal model of LBM by using a passive scalar approach for temperature.

The study of natural convection in an enclosure has grabbed massive attention because of its huge engineering and industrial applications. Solar power collectors, heat exchangers, crystal growth in liquids, processing of food and material, storage of grain, and safety of nuclear reactors are the areas of some of its applications [10,11]. The physics governing such buoyancy-driven flow often becomes complicated with the coupling between the fluid and thermal transport phenomena. Heat transfer in an enclosure with a body at the center also has relevance in modeling of baffle as a heat transfer controlling device [12] and in constructions of building in natural cooling flow [13]. It is seen that the central core of the stagnant fluid hinders the convective heat transfer in the cavity. The study by Bhave et al. [14] explores the cavity with single adiabatic obstacle and concluded that there exists an optimum size of obstacle where the heat transfer enhancement takes place due to convection. However, above that solidity ratio, deterioration in the heat transfer was observed. Similarly, Merrikh and Mohamad [15] also used adiabatic obstacle in the enclosure as means of heat transfer enhancement. However, House et al. [16] restricted themselves in the qualitative studies of centrally placed solid body with different conductivities on the enclosure but their study lacked the strict quantification.

Xu et al. [17] carried out an experiment to observe thermal flow around a square obstruction in a differentially heated cavity. Merrikh et al. [18] studied the comparison between the pore level and porous medium model for natural convection in a nonhomogeneous enclosure. David and Laurat [19] drew an analogy between wall channeling effects in porous media as well as in thermal convection loop. Roslan et al. [20] analyzed the conjugate natural convection heat transfer in a differentially heated square enclosure containing a conductive polygon obstacle. Ha et al. [21] used a spectral multidomain method to handle a square obstacle located at the center of enclosure. Hussain and Hussein [22] investigated the effect of inserting a rotating cylinder at different locations vertically inside a differentially heated square cavity. From the literature review, it is observed that the effect of multiple obstacles at different locations using Lattice Boltzmann method is not studied.

In the present work, different number of obstacles in a square enclosure is considered. In the case of single obstacle, various sizes of obstacle are considered and optimum size is obtained for higher heat transfer rate. The primary objective is to demarcate the comparison between the presences of obstacle in and out of the conduction dominant zone in the differentially heated square enclosure. Results are obtained for various Rayleigh numbers for all the cases at fixed Prandtl number. The laminar flow with steady-state condition is considered for the present study.

2 Problem Description

The schematic of the problems considered in this study is shown in Figs. 1(*a*)–1(*c*). In all cases, the top and bottom walls of the cavity are adiabatic while the side walls are at isothermal conditions. The left side wall ($T = T_h$) is at higher temperature than the right side wall ($T = T_c$). All the boundaries (walls) of the cavity are stationary. Three different cases are considered based on the number of obstacles. First, the code is validated for a cavity without obstacle. Next, case 1 is studied with the centrally placed single obstacle inside the center of the cavity as shown in Fig. 1(*a*). Further, the effect of the size of the obstacle is studied

[1]Corresponding author.

Contributed by the Heat Transfer Division of ASME for publication in the Journal of Thermal Science and Engineering Applications. Manuscript received April 2, 2018; final manuscript received October 26, 2018; published online February 6, 2019. Assoc. Editor: Yit Fatt Yap.

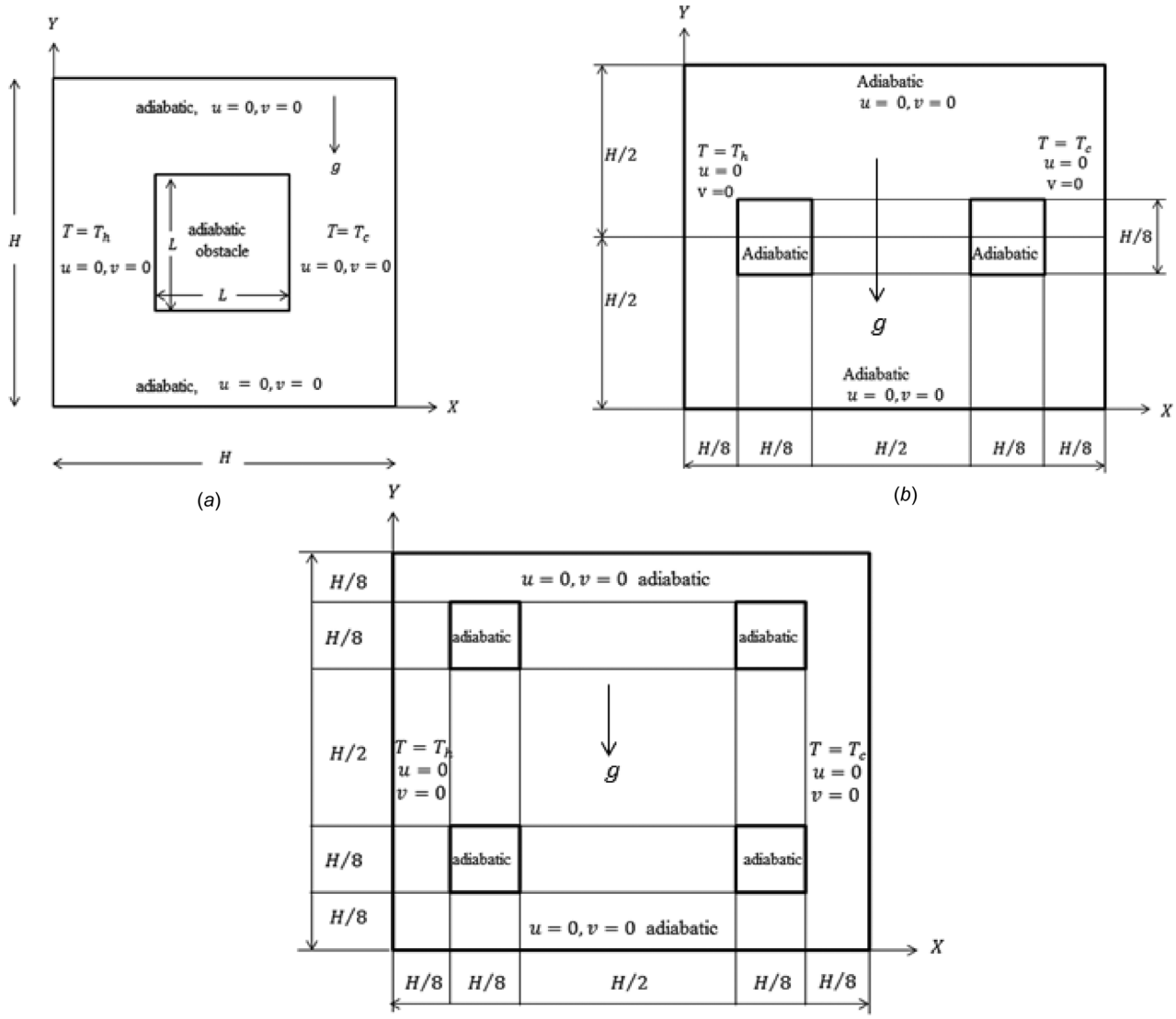

Fig. 1 Schematic of the cavity with boundary conditions: (*a*) single obstacle, (*b*) two obstacles, and (*c*) four obstacles

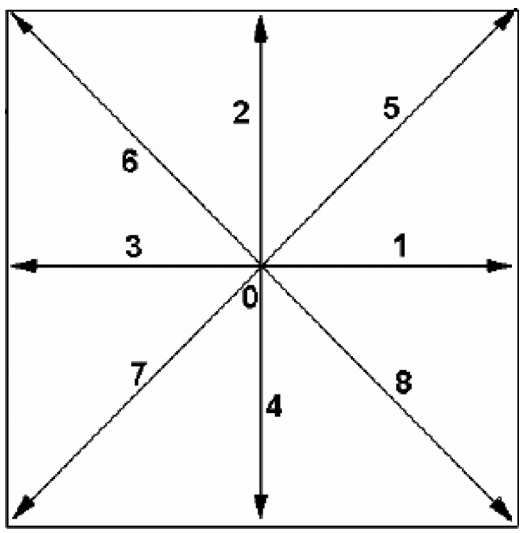

Fig. 2 *D2Q9* Lattice arrangement

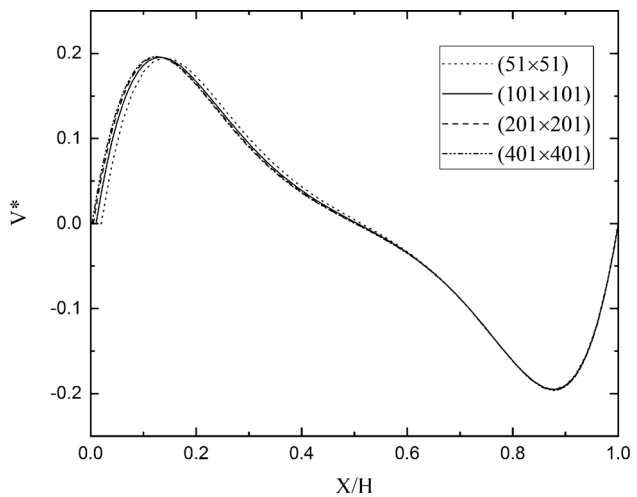

Fig. 3 Change in dimensionless vertical velocity at different lattice sizes

Table 1 Lattice size independence test for Ra = 10^4

Pr = 0.71		
Lattice size	$\overline{Nu_0}$	% change in $\overline{Nu_0}$
51×51	2.1713	–
101×101	2.2139	1.962
201×201	2.2161	0.099
401×401	2.2170	0.040

with respect to parameter ϕ (the ratio of height of the obstacle (L) to the height of the cavity (H), i.e., $\phi = L/H$). In case 2, the study is extended for two adiabatic obstacles placed at the midheight of the cavity with its width $H/8$ as shown in Fig. 1(*b*). Furthermore, case 3 deals with the cavity with four numbers of obstacles present in it as shown in Fig. 1(*c*). The size of the obstacle is equal to the size as discussed in case 2.

2.1 The Lattice Boltzmann Equation. The present work uses LBM to simulate momentum and energy transfer. LBM governing equations for velocity and temperature fields are shown in discretized form in Eqs. (1) and (2), respectively [19]. The two-dimensional *D2Q9* model is employed to solve fluid flow and temperature fields in the bounded domain. *D2Q9* refers to a kind of lattice arrangement where D represents space dimension (2: for 2 dimensions) and Q represents the number of discrete velocities (9: for 9 directions). Each lattice node comprises eight neighbors connected by eight links as shown in Fig. 2

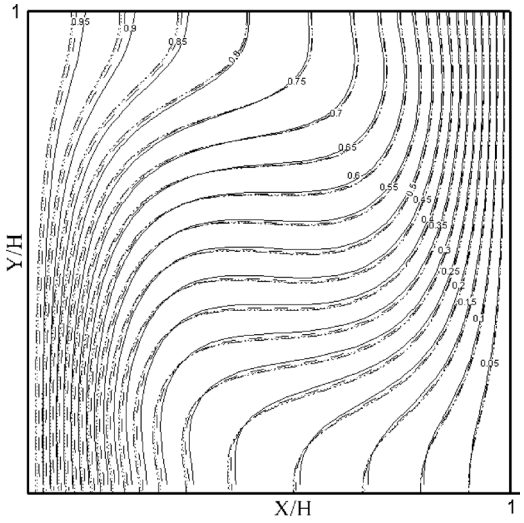

Fig. 4 Isotherms at different lattice sizes

$$f_i(x + c_i\Delta t, t + \Delta t) - f_i(x, t) = -\frac{f_i(x, t) - f_i^{eq}(x, t)}{\tau_v} + \Delta t F_i \quad (1)$$

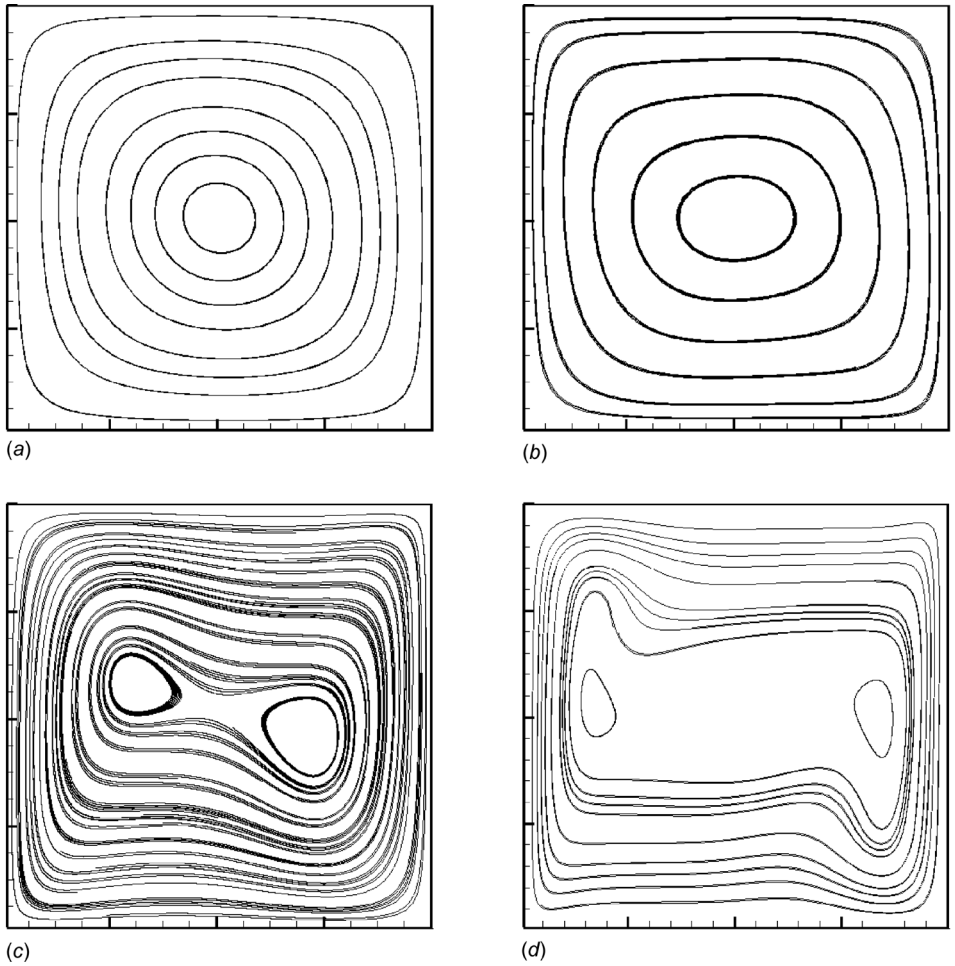

Fig. 5 Streamline patterns of different Ra: (*a*) Ra = 10^3, (*b*) Ra = 10^4, (*c*) Ra = 10^5, and (*d*) Ra = 10^6

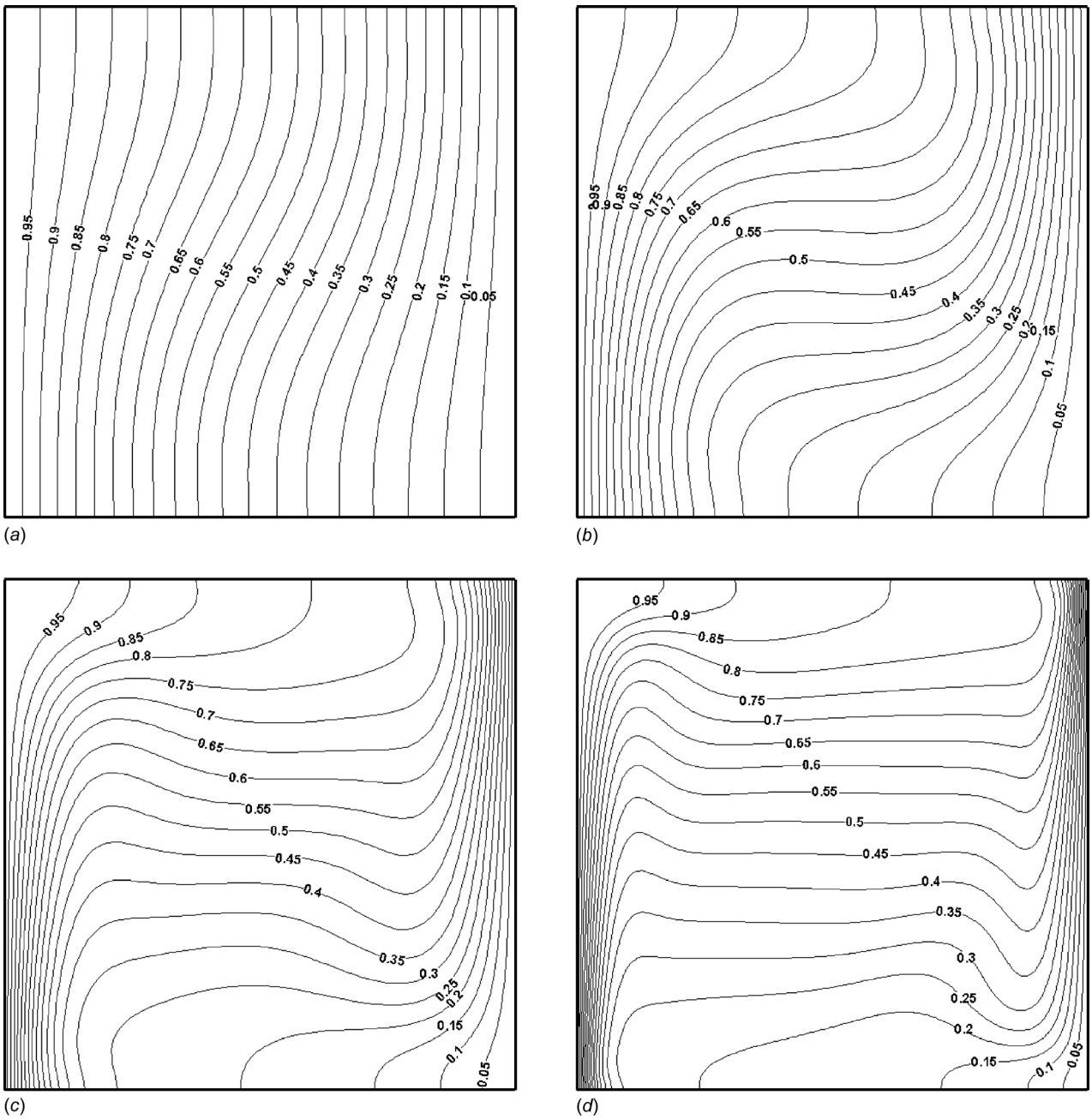

Fig. 6 Isotherm patterns of different Ra: (*a*) Ra = 10^3, (*b*) Ra = 10^4, (*c*) Ra = 10^5, and (*d*) Ra = 10^6

$$g_i^{\mathrm{eq}} = w_i' T(x,t)\left[1 + \frac{c_i u}{c_s^2}\right] \tag{2}$$

The equilibrium distribution function for velocity and temperature can be written as

$$f_i^{\mathrm{eq}} = w_i \rho\left[1 + 3\frac{c_i u}{c^2} + \frac{9}{2}\frac{[c_i u]^2}{c^4} - \frac{3}{2}\frac{u.u}{c^2}\right] \tag{3}$$

$$g_i^{\mathrm{eq}} = w_i T(x,t)\left[1 + \frac{c_i u}{c_s^2}\right] \tag{4}$$

where f_i,f_i^{eq}, τ_v, and F_i are particle distribution function, equilibrium particle distribution function, relaxation time for velocity field, and external force in all i directions, respectively. Further, ρ and $T(x,t)$ are the local density and temperature in the computational domain, whereas c_s is the lattice speed of sound and is given by $c_s = c/\sqrt{3}$, in which c refers to lattice streaming speed. Here, c can be further interpreted as $c = \Delta x/\Delta t$ where $\Delta x = \Delta t = 1$, where w_i represents weight for equilibrium distribution function and is given by

$$w_i = \begin{cases} \frac{4}{9} & i = 0 \\ \frac{1}{9} & i = 1,2,3,4 \\ \frac{1}{36} & i = 5,6,7,8 \end{cases} \tag{5}$$

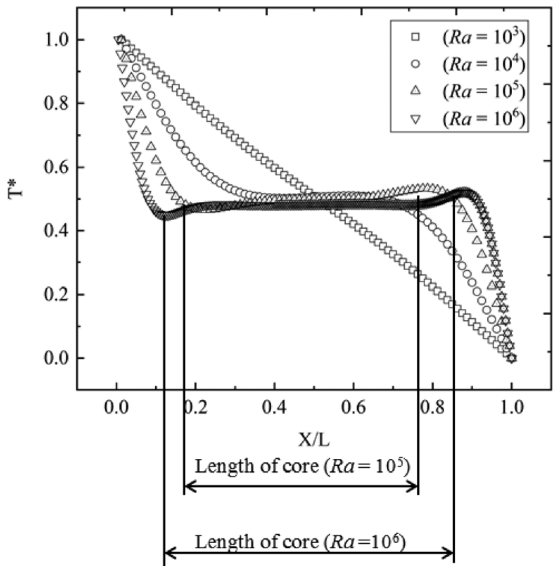

Fig. 7 Temperature variation along the horizontal centerline (*Y/H* = 0.5)

Table 2 Code validation at different Rayleigh numbers

Ra		10^3	10^4	10^5	10^6
U_{max}	Present	3.660	16.180	35.625	64.465
	Davis [23]	3.469	16.178	34.730	64.630
	Dixit and Babu [10]	3.652	16.163	35.521	64.186
Y/H	Present	0.814	0.832	0.858	0.852
	Davis [23]	0.813	0.823	0.855	0.850
	Dixit and Babu [10]	0.813	0.828	0.855	0.849
V_{max}	Present	3.702	19.567	68.660	219.800
	Davis [23]	3.697	19.617	68.590	219.360
	Dixit and Babu [10]	3.682	19.569	68.655	219.866
X/H	Present	0.176	0.126	0.065	0.0376
	Davis [23]	0.178	0.119	0.066	0.0379
	Dixit and Babu [10]	0.171	0.125	0.066	0.0371
$\overline{Nu}$	Present	1.112	2.247	4.540	8.786
	Davis [23]	1.118	2.243	4.519	8.800
	Dixit and Babu [10]	1.121	2.286	4.546	8.652
$\overline{Nu_0}$	Present	1.113	2.216	4.524	8.810
	Davis [23]	1.117	2.238	4.509	8.817
	Dixit and Babu [10]	1.127	2.247	4.522	8.805

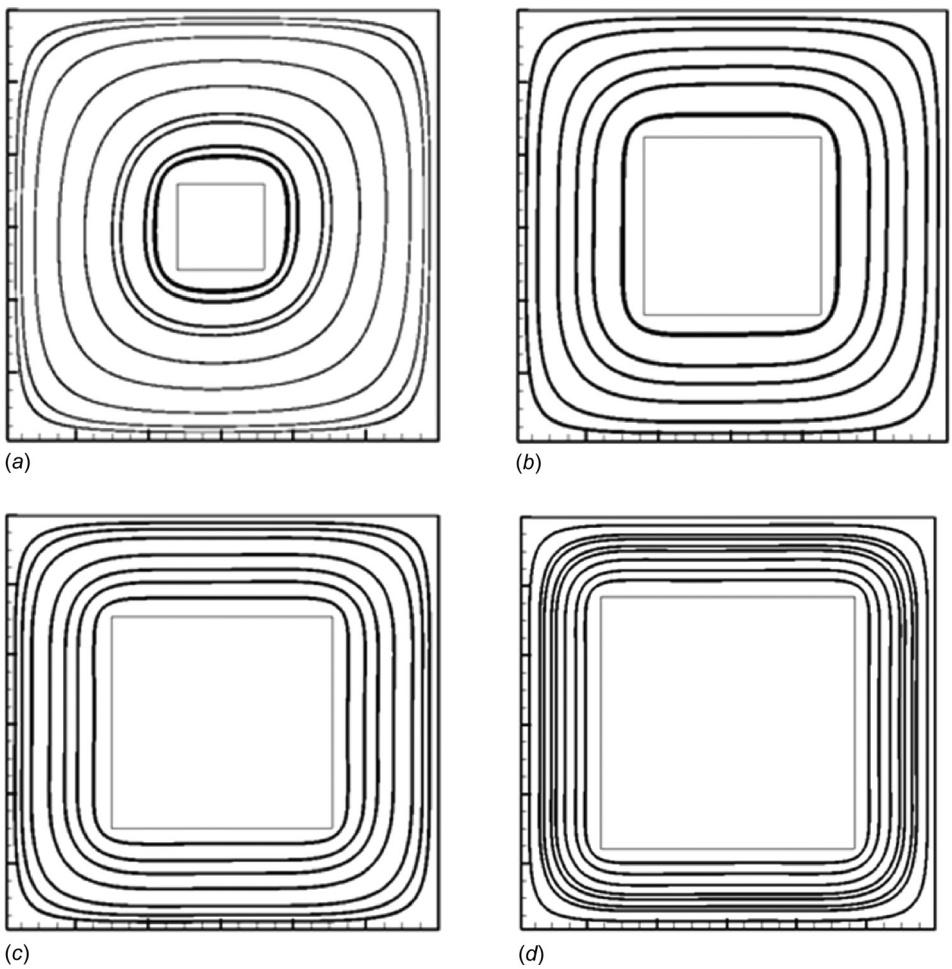

Fig. 8 Streamline patterns at Ra = 10^3: (*a*) $\phi = 0.20$, (*b*) $\phi = 0.40$, (*c*) $\phi = 0.50$, and (*d*) $\phi = 0.60$

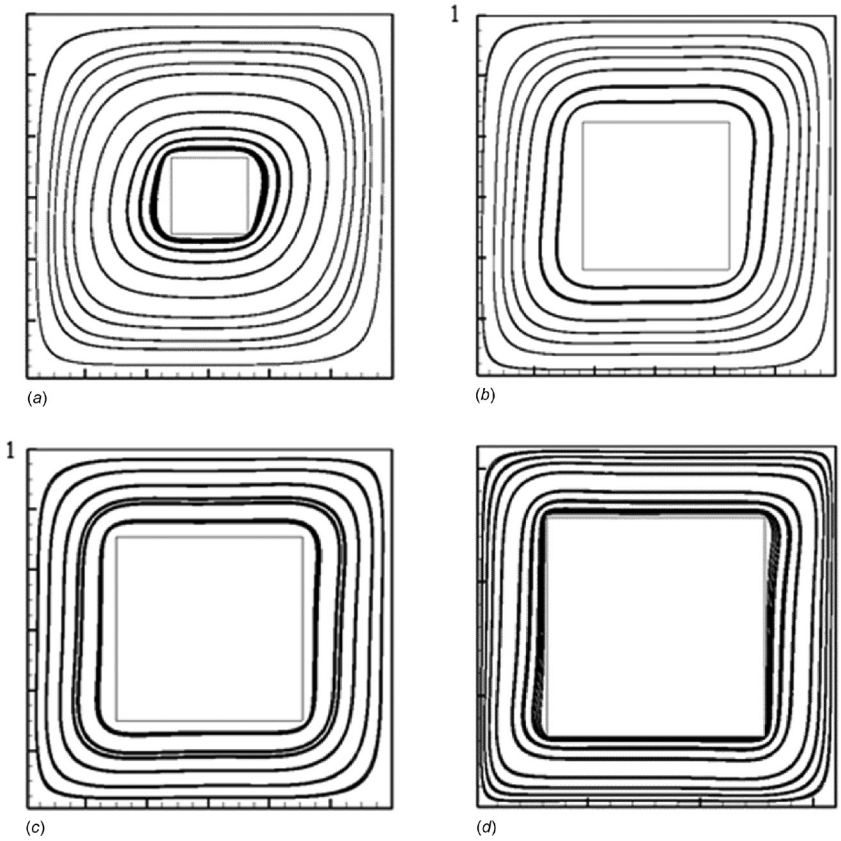

Fig. 9 Streamline patterns at Ra = 10^4: (*a*) $\phi = 0.20$, (*b*) $\phi = 0.40$, (*c*) $\phi = 0.50$, and (*d*) $\phi = 0.60$

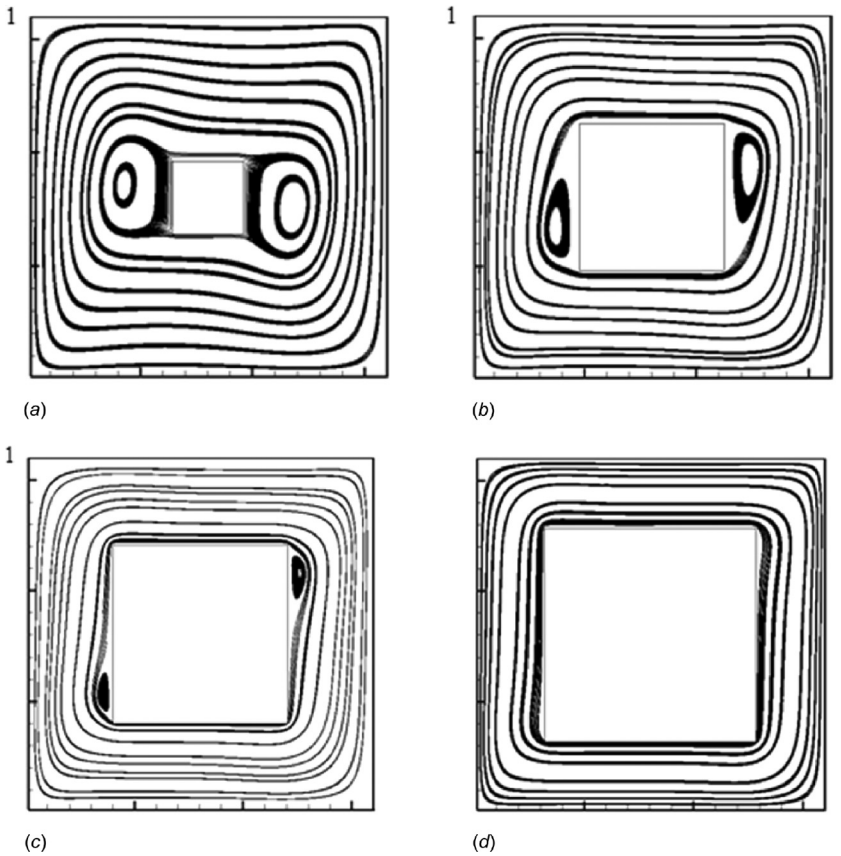

Fig. 10 Streamline patterns at Ra = 10^5: (*a*) $\phi = 0.20$, (*b*) $\phi = 0.40$, (*c*) $\phi = 0.50$, and (*d*) $\phi = 0.60$

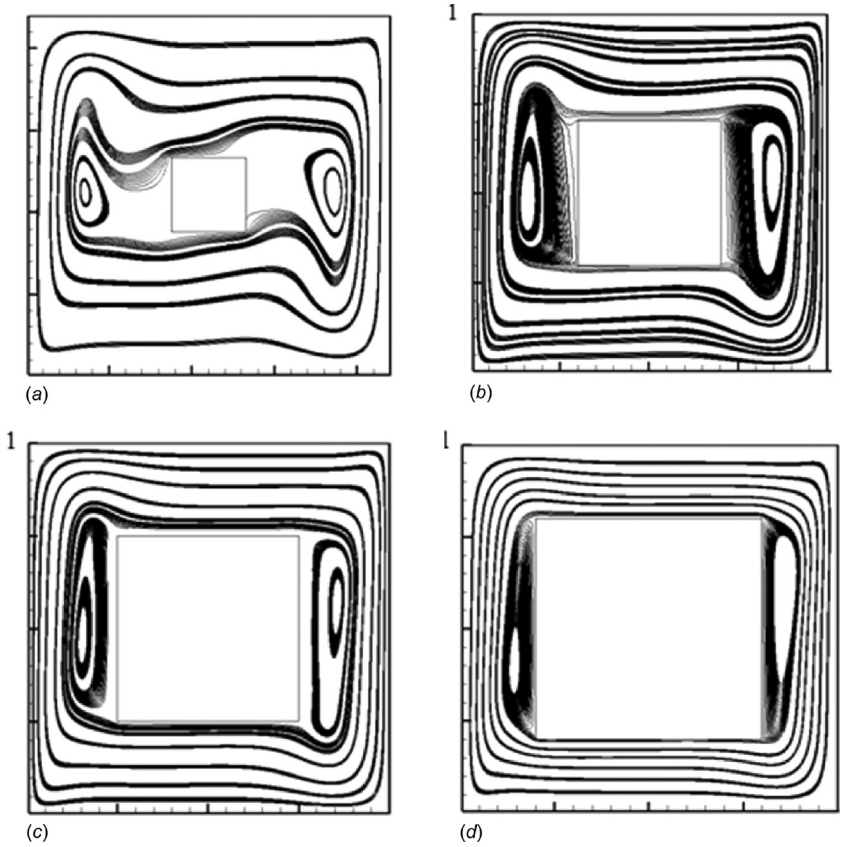

Fig. 11 Streamline patterns at Ra = 10^6: (*a*) $\phi = 0.20$, (*b*) $\phi = 0.40$, (*c*) $\phi = 0.50$, and (*d*) $\phi = 0.60$

And the discrete velocity vector c_i is given by

$$c_i = \begin{cases} c_0 = (0,0) i = 0 & \\ c_i = c(\cos\theta_i,\ \sin\theta_i) & \theta_i = (i-1)\dfrac{\pi}{2} \\ & i = 1,2,3,4 \\ c_i = c\sqrt{2}(\cos\theta_i,\ \sin\theta_i) & \theta_i = (i-5)\dfrac{\pi}{2} + \dfrac{\pi}{4} \\ & i = 5,6,7,8 \end{cases} \tag{6}$$

The relaxation time τ_v for the momentum equation and relaxation time τ_c for the temperature field are calculated using the following equations [18]:

$$\nu = \left[\tau_v - \frac{1}{2}\right] {c_s}^2 \Delta t \tag{7}$$

$$\alpha = \left[\tau_c - \frac{1}{2}\right] {c_s}^2 \Delta t \tag{8}$$

The properties such as density, momentum, and temperature can be obtained as [24]

$$\rho(x,t) = \sum_i f_i(x,t) \tag{9}$$

$$\rho u(x,t) = \sum_i c_i f_i(x,t) \tag{10}$$

$$T(x,t) = \sum_i g_i(x,t) \tag{11}$$

The LBM is regulated by two basic processes, i.e., collision and streaming. The particles that reside in each lattice collide with each other, thus producing change in the kinetic energy is called collision while their movement from one lattice link to another is called streaming. Mathematically, these two processes can be understood as

$$\text{Collision step}: f_i(x,y,t+\Delta t) = f_i(x,y,t)[1-\omega] + \omega f_i^{eq}(x,y,t) \tag{12}$$

$$\text{Streaming step}: f_i(x,y,t+\Delta t) = f_i(x,y,t) \tag{13}$$

It is very important to understand the coupling between the momentum and energy equations in order to solve the problems accurately. Since the flow is driven by the temperature gradient, the buoyance force is estimated and added in the collision term [19]

$$F = \frac{w_i F c_i}{{c_s}^2} \tag{14}$$

F in Eq. (14) can be written as

$$F = \rho g \beta (T - T_m) \tag{15}$$

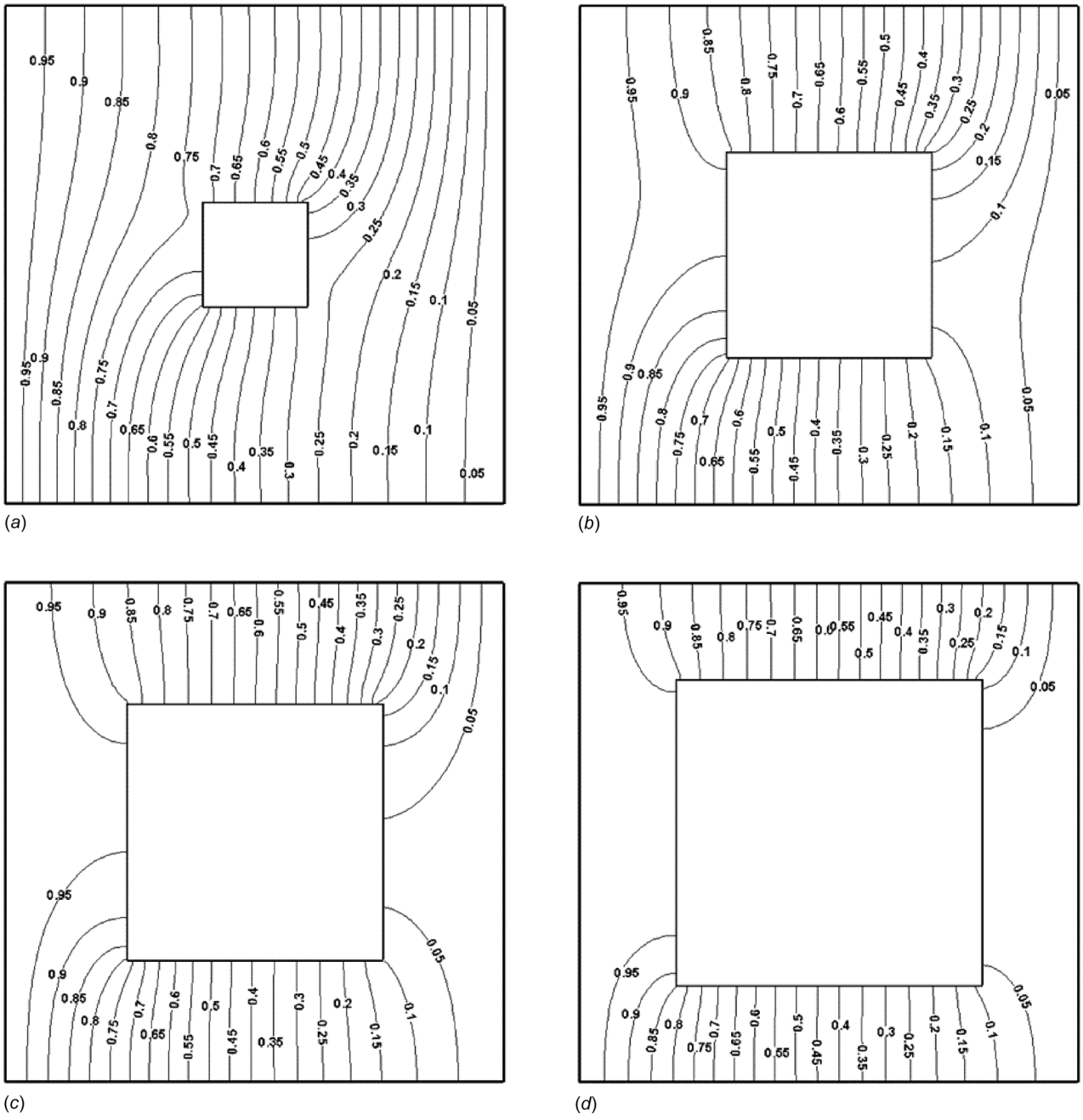

Fig. 12 Isotherms obtained at various aspect ratios at Ra = 10^3: (*a*) $\phi = 0.20$, (*b*) $\phi = 0.40$, (*c*) $\phi = 0.50$, and (*d*) $\phi = 0.60$

Table 3 Average Nusselt number along hot wall at various ϕ for various Ra

Rayleigh number	Average Nusselt number along the hot wall ($\overline{Nu_0}$)				
10^3	$\phi = 0$	$\phi = 0.03$	$\phi = 0.05$	$\phi = 0.10$	$\phi = 0.30$
	1.1130	1.1105	1.1073	1.0912	0.9050
10^4	$\phi = 0$	$\phi = 0.10$	$\phi = 0.15$	$\phi = 0.20$	$\phi = 0.30$
	2.2161	2.2404	2.2417	2.2433	2.2200
10^5	$\phi = 0$	$\phi = 0.20$	$\phi = 0.40$	$\phi = 0.50$	$\phi = 0.60$
	4.5248	4.5665	4.6252	4.6263	4.4867
10^6	$\phi = 0$	$\phi = 0.40$	$\phi = 0.50$	$\phi = 0.60$	$\phi = 0.70$
	8.8100	8.9085	8.9706	8.9809	8.7386

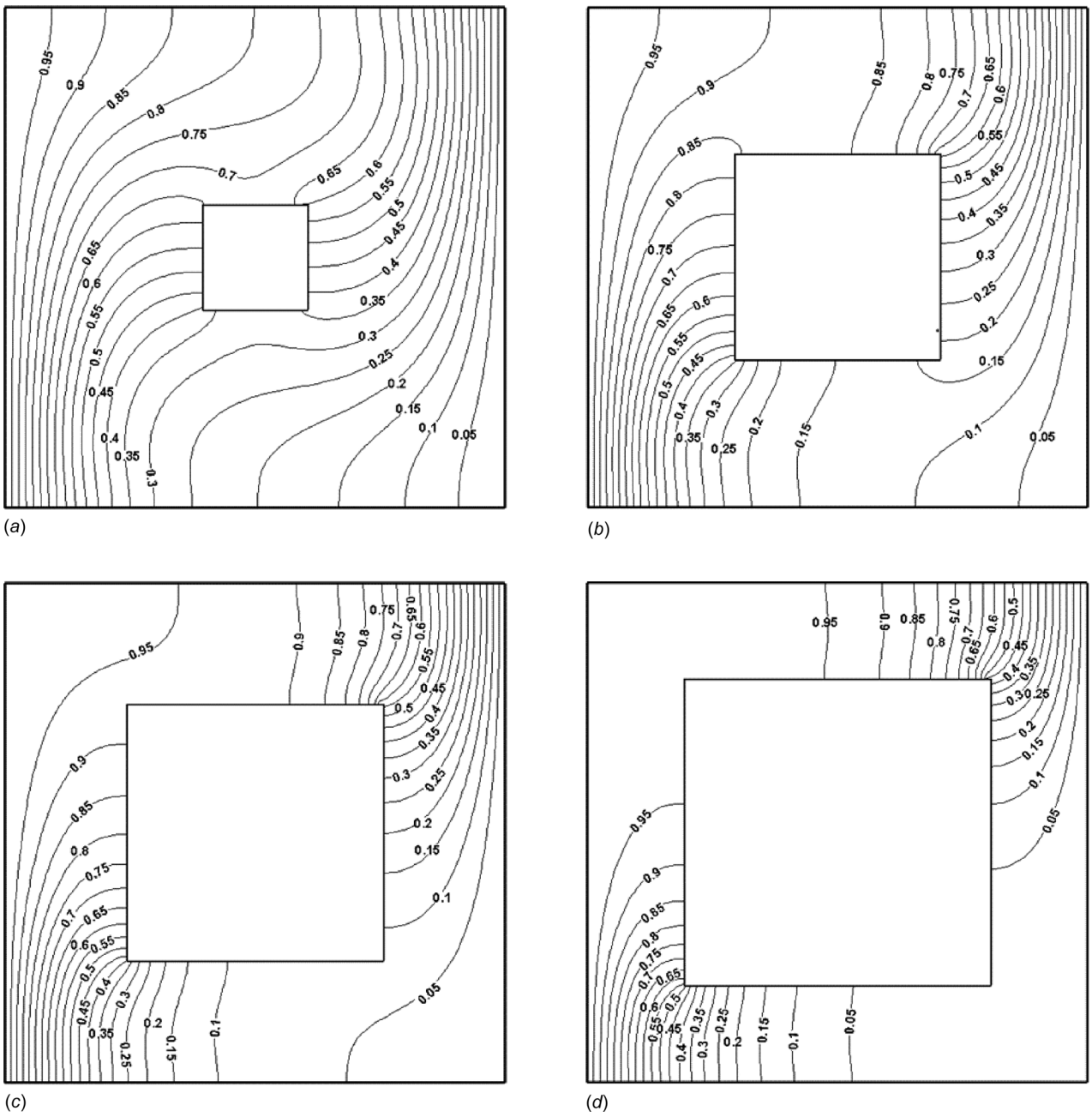

Fig. 13 Isotherms obtained at various aspect ratios at Ra = 10^4: (*a*) $\phi = 0.20$, (*b*) $\phi = 0.40$, (*c*) $\phi = 0.50$, and (*d*) $\phi = 0.60$

In the present study, Rayleigh number and Prandtl number are two parameters that govern this type of flow and are thus defined as

$$\mathrm{Ra} = \frac{g\beta\Delta T H^3}{\alpha\upsilon} \tag{16}$$

$$\mathrm{Pr} = \frac{\upsilon}{\alpha} \tag{17}$$

Average Nusselt number along the hot wall is used as a parameter to signify the magnitude of convective heat transfer in the cavity and is defined as

$$\overline{\mathrm{Nu}_0} = \int_0^1 -k\frac{\partial T^*}{\partial X^*}\partial Y^* \tag{18}$$

where α, H, p_∞, ρ, β, g, υ, k, and $\Delta T(= T - T_m)$, $X^*(= (X/H))$ and $Y^*(= (Y/H)))$ are thermal diffusivity, height of the domain, reference pressure, density, thermal expansion coefficient, acceleration due to gravity, kinematic viscosity, thermal conductivity of fluid, temperature difference, dimensionless length in X and Y directions, respectively. The gravity acts in the downward direction and T_m is the mean temperature, which is defined as the average of the two isothermal walls.

2.2 Boundary Conditions

2.2.1 Velocity Boundary Conditions. Since all four boundaries of the cavity and the obstacle are at rest, no-slip boundary conditions at the walls are applied. The no-slip boundary conditions in LBM can be implemented as bounce-back boundary condition where the distribution function coming in is equated in

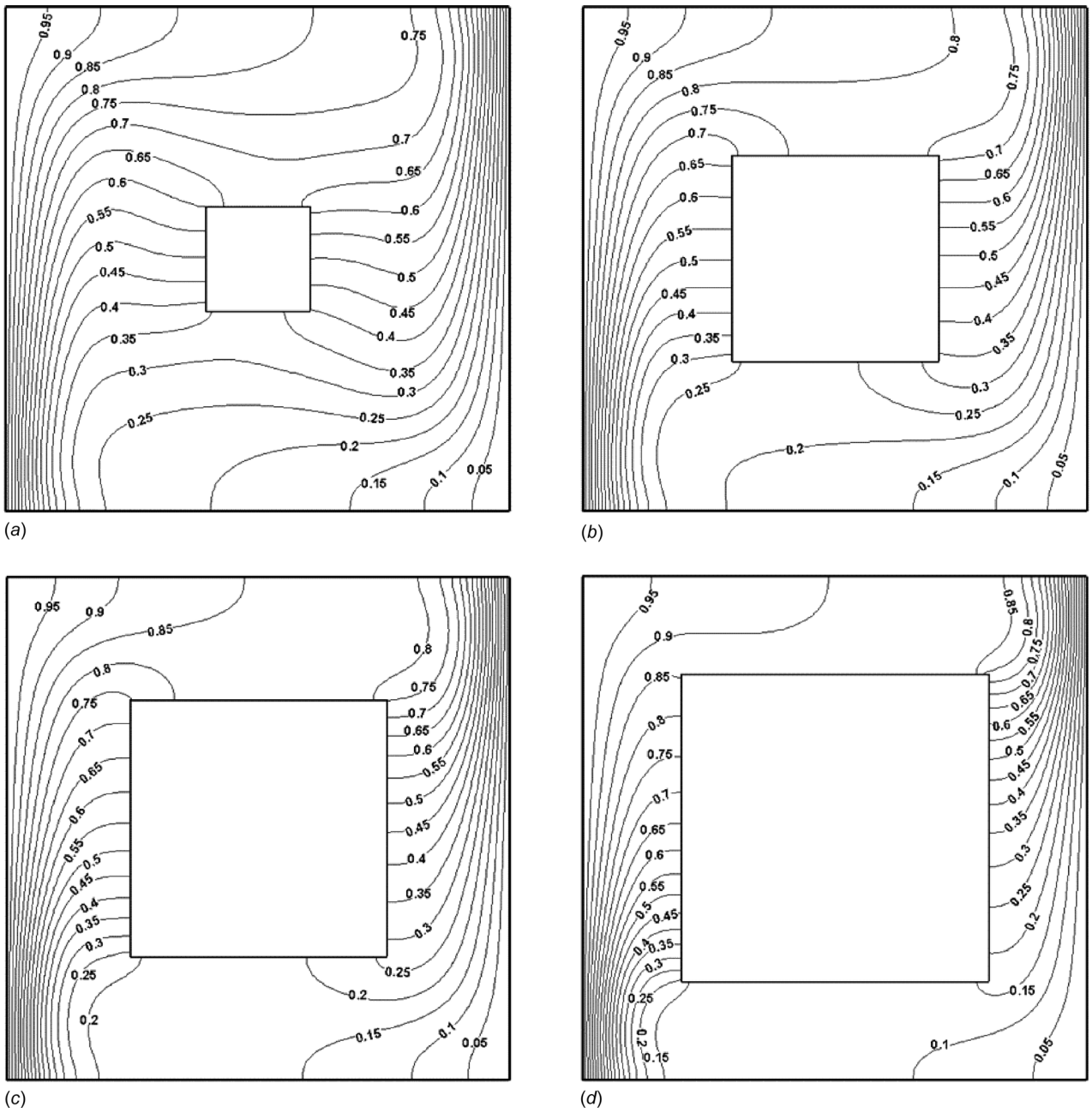

Fig. 14 Isotherms obtained at various aspect ratios at Ra = 10^5: (*a*) $\phi = 0.20$, (*b*) $\phi = 0.40$, (*c*) $\phi = 0.50$, and (*d*) $\phi = 0.60$

terms of distribution function going out after collision. For example in the west boundary

$$\begin{aligned} f_1(1,j) &= \tilde{f}_3(1,j) \\ f_5(1,j) &= \tilde{f}_7(1,j) \\ f_8(1,j) &= \tilde{f}_6(1,j) \end{aligned} \tag{19}$$

where $\tilde{f}_i$ denotes the post collision and streaming distribution functions, similar bounce-back boundary conditions can be applied at all the boundaries.

2.2.2 Temperature Boundary Conditions. The vertical walls are maintained at two different temperatures, whereas horizontal walls are maintained at adiabatic temperatures. The Dirichlet boundary condition for hot wall in LBM can be implemented with flux conservation equation [1]

$$g_1(1,j) - g_1^{\text{eq}}(1,j) + g_3(1,j) - g_3^{\text{eq}}(1,j) = 0 \tag{20}$$

Since $g_i^{\text{eq}} = w(i) \times \theta_w$ and $g_1(1,j)$ is incoming population, which is unknown and thus it should be expressed in terms $g_3(1,j)$, which lend us to write Eq. (20) as

$$\begin{aligned} g_1(1,j) &= g_1^{\text{eq}}(1,j) - g_3(1,j) + g_3^{\text{eq}}(1,j) \\ g_1(1,j) &= 0.5 \times \theta_w - g_3(1,j) \end{aligned} \tag{21}$$

For cold wall, $\theta_w = 0$, then the $g_3(m,j)$, can be written as

$$g_3(m,j) = 0 - g_1(m,j) \tag{22}$$

The Neumann boundary condition at top and bottom walls of the cavity and in all the walls of the obstacle can be implemented

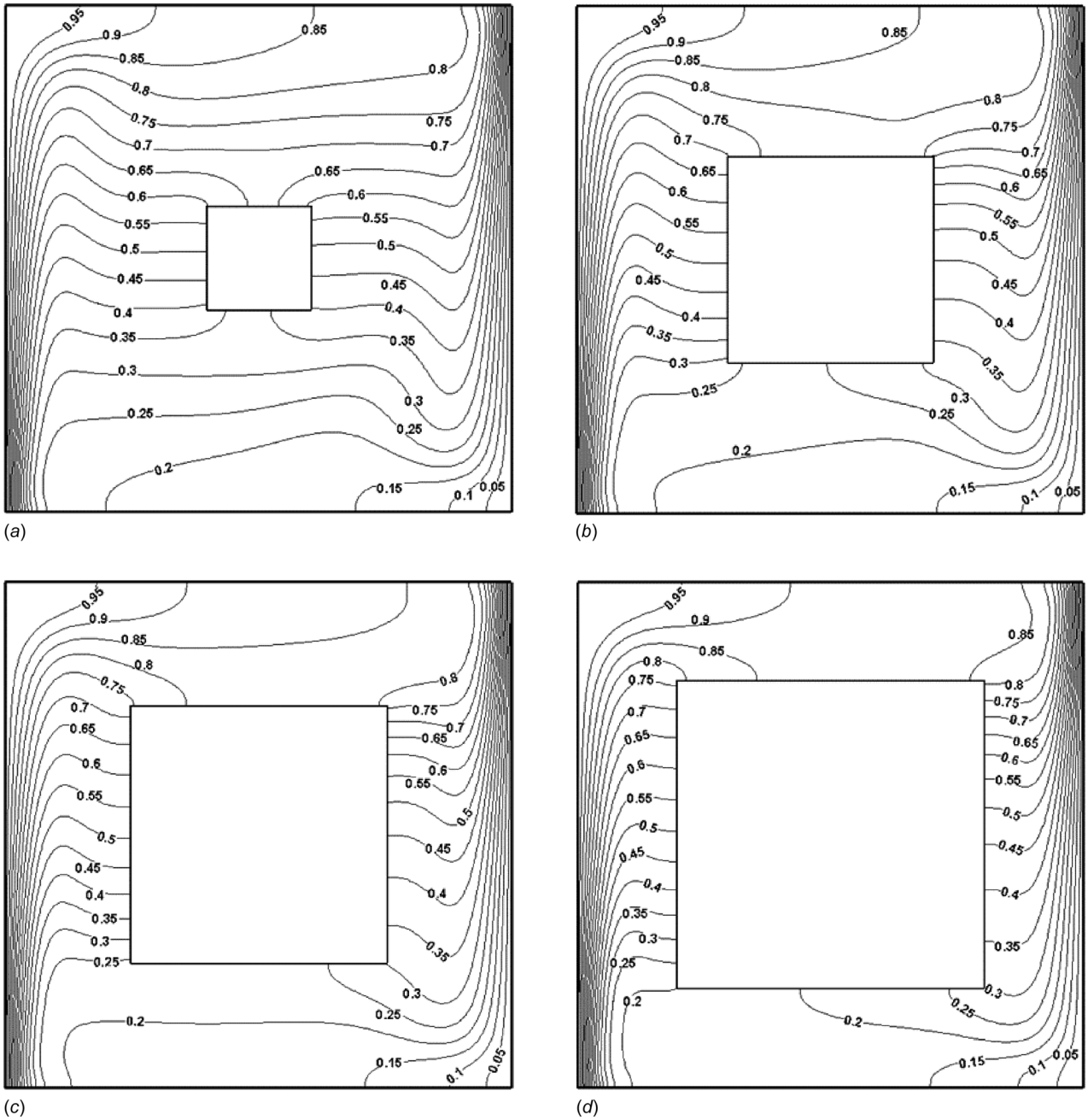

Fig. 15 Isotherms obtained at various aspect ratios at Ra = 10^6: (*a*) $\phi = 0.20$, (*b*) $\phi = 0.40$, (*c*) $\phi = 0.50$, and (*d*) $\phi = 0.60$

with bounce-back boundary conditions in LBM, which is same as Eq. (19) with g in place of f.

3 Results and Discussion

3.1 Lattice Size Independence Study. The lattice size independence study for $\mathrm{Ra} = 10^4$ is shown in Table 1. The different numbers of lattices are taken into consideration for this study. With the change in lattice size, the change in Nusselt number is observed. Further dimensionless vertical velocity ($V^* = V/U_0$; $U_0 = \sqrt{g\beta\Delta TH}$) is plotted in Fig. 3. The isotherms are also overlapped to observe the change with the lattice size as shown in Fig. 4. The lattice size with very less change in Nusselt number is taken as the optimum size for the study. The lattice size independence study is also carried out for other Ra. For high Ra, the finer mesh size is used. All the results presented here are grid independent.

3.2 Code Validation: Cavity Without an Obstacle. In this section, to validate the code, differentially heated cavity is discussed without the presence of obstacle. Figures 5 and 6 show the streamline and isotherm patterns for different Rayleigh number $10^3 \leq \mathrm{Ra} \leq 10^6$. The streamline and isotherm patterns are plotted along with the tabulation of Nusselt number for different Rayleigh number. In all the cases, streamline patterns show a clockwise movement in the cavity. Figure 7 shows the dimensionless temperature ($T^* = (T - T_c/T_h - T_c)$) variation along the horizontal centerline ($Y/H = 0.5$) of the cavity for Rayleigh number $10^3 \leq \mathrm{Ra} \leq 10^6$. Table 2 illustrates the comparison of the present work with the well-established solution of Dixit and

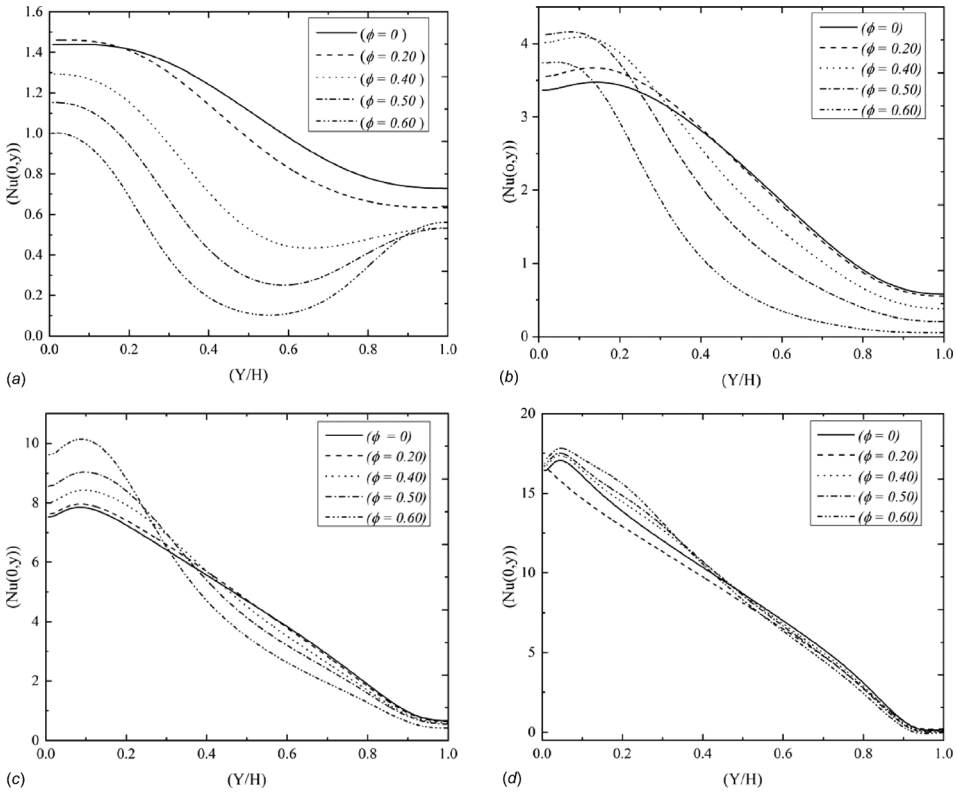

Fig. 16 Nusselt number variation along the hot wall: (*a*) Ra = 10^3, (*b*) Ra = 10^4, (*c*) Ra = 10^5, and (*d*) Ra = 10^6

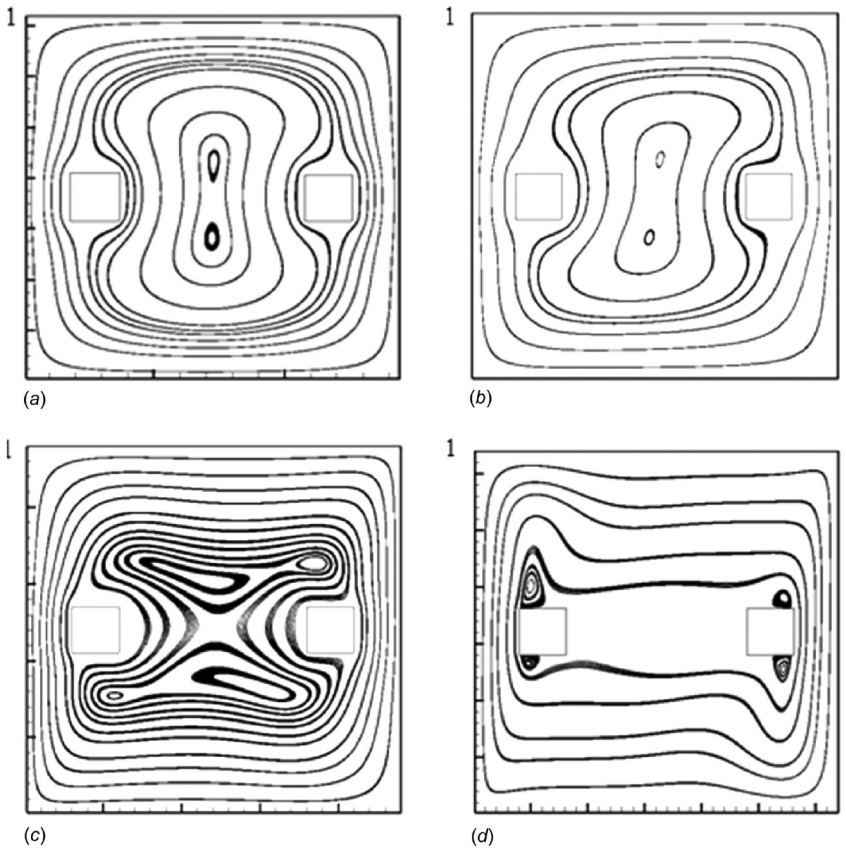

Fig. 17 Streamline patterns for cavity with two obstacles: (*a*) Ra = 10^3, (*b*) Ra = 10^4, (*c*) Ra = 10^5, and (*d*) Ra = 10^6

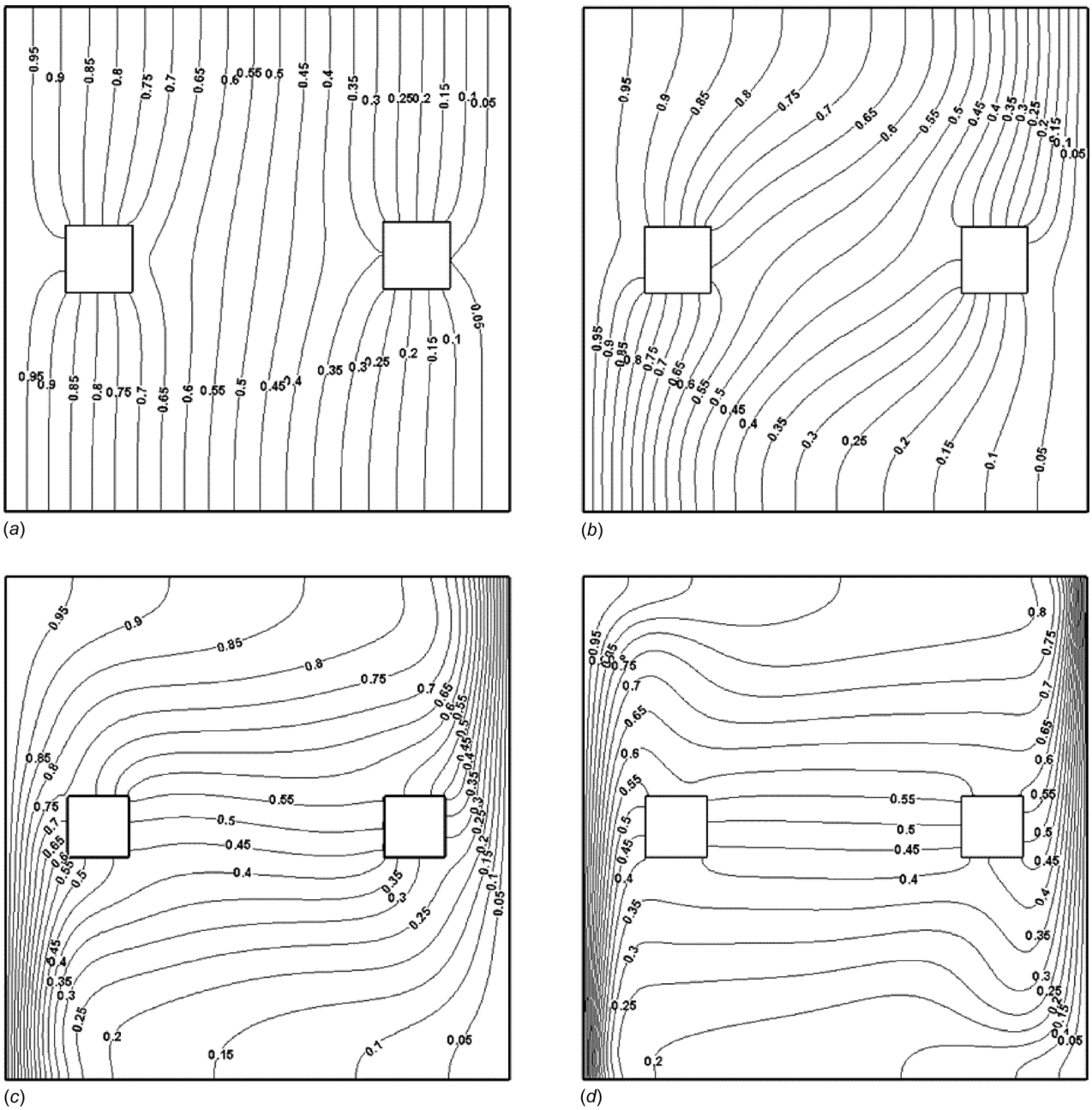

Fig. 18 Isotherm patterns for cavity with two obstacles: (*a*) Ra = 10^3, (*b*) Ra = 10^4, (*c*) Ra = 10^5, and (*d*) Ra = 10^6

Babu [10], and De Vahl Davis [23]. The variation of the magnitude and location of the maximum X-component velocity (U_{max}) along the vertical centerline ($X/H = 0.5$), Y-component velocity (V_{max}) along the horizontal centerline ($Y/H = 0.5$), average Nusselt number ($\overline{Nu}$) (i.e., average of Nusselt number along the hot and cold wall), and average Nusselt number along the hot wall ($\overline{Nu_0}$) for different Ra are shown. The results show good agreement with published data.

Figures 5 and 6 indicate the extent of center of fluid not participating in convection across the enclosure or the region in the cavity where the isotherms are parallel to each other. Geometrically, it is a rectangular region. This implies heat conduction takes place vertically within the region. Therefore, from the figures of isotherms (Fig. 6), it can be inferred that the core region expands with increase in Rayleigh number. The flow consists of two distinct regimes: a parallel flow in core region and nonparallel flow near the ends of cavity.

3.3 Cavity With Single Obstacle at Geometric Center. In this section, a single obstacle present in the center of the cavity is considered. The results are obtained in the form of streamlines and isotherms for a single obstacle present in the center of the cavity. Figures 8–11 depict the streamline patterns of Ra = 10^3, 10^4, 10^5, and 10^6 at different aspect ratios. The different aspect ratios (ϕ) considered here are 0.2, 0.4, 0.5 and 0.6. At low Rayleigh number (Ra = 10^3 and 10^4), formation of vortex is not observed for all aspect ratios whereas, at higher Rayleigh number (Ra = 10^5 and 10^6), the vortices are noticeable for all aspect ratios except only for the case of $\phi = 0.6$. At low Ra, the streamline patterns are in circular shape and are uniformly distributed. This is a signal of very weak convection, whereas nonuniform distribution of streamline patterns and elongation in circular cells at high Ra indicates the domination of convection in the outer (near wall) zone and domination of conduction in the core zone. When the size of the adiabatic obstacle is relatively large ($\phi = 0.60$), there is no

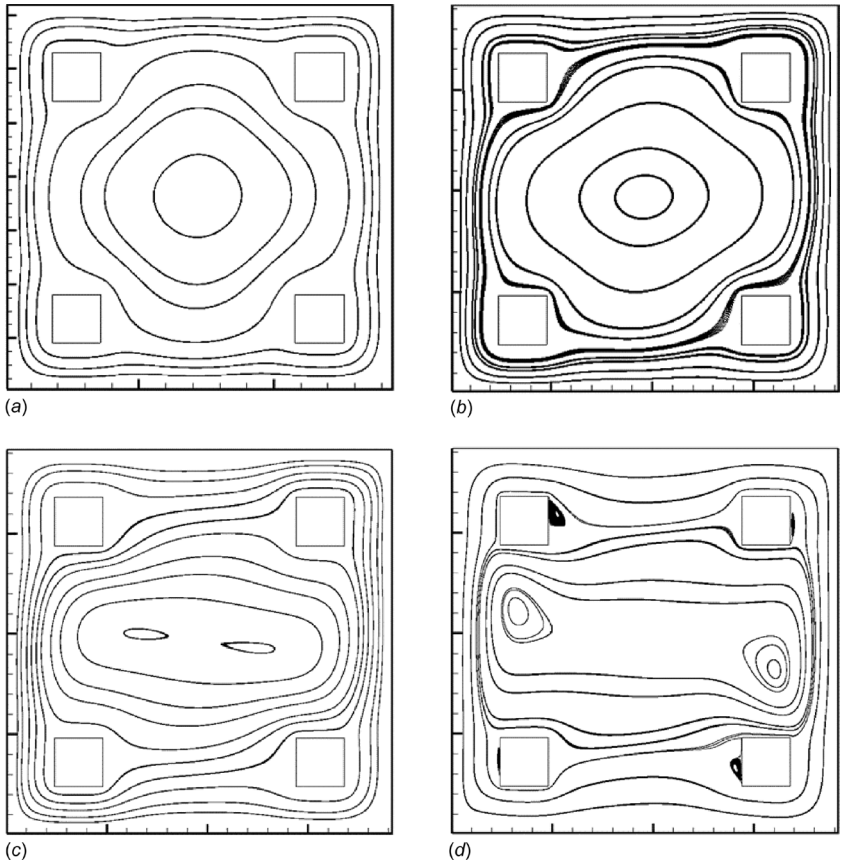

Fig. 19 Streamline patterns for cavity with four obstacles: (*a*) Ra = 10^3, (*b*) Ra = 10^4, (*c*) Ra = 10^5, and (*d*) Ra = 10^6

secondary flow developed as seen in Fig. 10(*d*) for Ra = 10^5. The core size for Ra = 10^5 is smaller than the core size for Ra = 10^6; therefore, appearance of recirculation zone is found in Fig. 11(*d*) and not in Fig. 10(*d*). This can be contributed to the fact that velocity components are significant (refer Table 2) to cause the recirculation of the flow at high Ra, as strong buoyancy force prevails and vortices formed are not completely enveloped. With further increase in obstacle size, the larger portion of the fluid in cavity is removed resulting insignificant convective flow, and higher flow resistance is observed as the obstacle reaches closer to the walls of the cavity.

The next part of the study with single obstacle present in cavity is to analyze the behavior of the isotherms for different Rayleigh numbers. Figure 12 shows the isotherms obtained at various aspect ratios at Ra = 10^3. For all ϕ values, there is a centrosymmetry isotherm pattern as similar to previous case. As discussed earlier, with increase in Rayleigh number conduction dominant region (stagnant core zone) increases, the value of ϕ at which the obstacle suppresses convective flow increase with Ra. For example, the value of $\phi = 0.2$ for Ra = 10^4 while $\phi = 0.6$ for Ra = 10^6 (See Table 3). However, as size of obstacle increases ($\phi \sim$ core zone), isotherms get pulled toward the obstacles as shown in Figs. 12–15 (i.e., the vertical isotherms remain no longer parallel). As a result, fluid flowing between the vertical walls of the cavity and adiabatic vertical sides of obstacle prevents vertical heat conduction. This statement can further be supported with the help of expression described by Bhave et al. [14] and is given as $Q \sim k_f\,(T_{\text{top}} - T_{\text{bottom}})$. This expression clearly elucidates that the difference in temperature ($T_{\text{top}} - T_{\text{bottom}}$) should be maximum to obtain maximum Q. When the size of obstacle is increased, T_{top} tends to become T_h and T_{bottom} tends to become T_c. This is valid till $\phi \sim$ core zone condition is satisfied. However, with further increase in length, this statement does not stay staunch as the larger portion of core zone is removed.

Figure 16 shows the Nusselt number variation along the hot wall for different Rayleigh numbers. Here, the adiabatic block acts as an insulator between hot and cold fluid in the upper and lower passages, respectively. No change in temperature in flowing fluid is observed in the passage. However, there is significant heat transfer from the fluid from the upper (lower) passage to right (left) passage. As fluid path changes the direction from upper (lower) passage to left (right) passage, the fluid loses (gains) heat significantly because of the fact that conduction path is very small (lower left corner and upper right corner) as compared to the length of the cavity. Therefore, the fluid approaching the hot wall (cold wall) is already heated (cooled) leading to the increase in the Nusselt number at bottom of the vertical as the fluid advects heat laterally.

At Ra = 10^3, the local Nusselt number is higher near the bottom of vertical wall. The Nusselt number tends to decrease with increase in Y/H (the distance along the vertical). The minimum local Nusselt number is found to occur at $Y/H = 0.5$ for $\phi = 0$. However, after reaching certain minimum value, it increases but the increment in local Nusselt number is less than the Nusselt number near the bottom of vertical wall. The Nusselt number trend observed at Ra = 10^3 is absent at high Rayleigh number. Value of Nusselt number is observed to decrease linearly with Y/H. The position of occurrence of maximum Nusselt number remains constant despite the change in values of ϕ at aforementioned Rayleigh number. The local Nusselt number increases with increase in ϕ at $Y/H < 0.1$, however this trend is absent beyond $Y/H > 0.1$. The large size obstacle present in cavity damps the fluid movement obstructing the proper motion of the fluid in cavity thereby decreases the convective heat transfer rate. Table 3

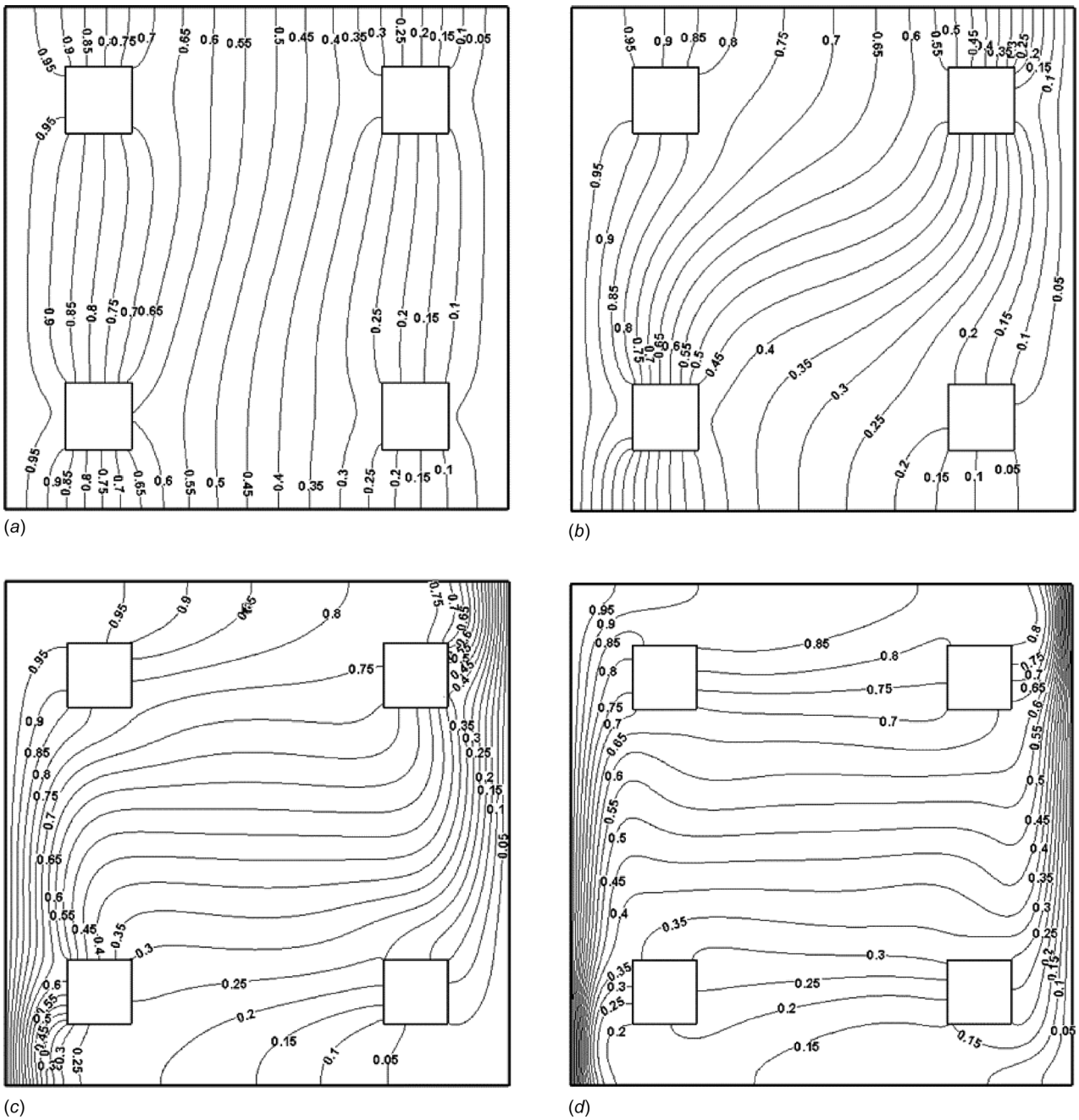

Fig. 20 Isotherms patterns for cavity with four obstacles: (*a*) Ra = 10^3, (*b*) Ra = 10^4, (*c*) Ra = 10^5, and (*d*) Ra = 10^6

Table 4 Nusselt number variation of cavity with the number of obstacles present

	Average Nusselt number at hot wall ($\overline{Nu_0}$)		
Rayleigh number	Without obstacle	With two obstacles	With four obstacles
10^3	1.1130	0.9305	0.8757
10^4	2.2161	1.3970	1.3170
10^5	4.5248	4.2994	3.7775
10^6	8.8100	8.7148	8.6841

depicts the change in average Nusselt number with the change in Rayleigh number for various values of ϕ.

3.4 Cavity With Two and Four Obstacles. This section deals with influence of adiabatic obstacles (2 and 4 in number) on the flow and thermal behaviors. Figure 17 represents the streamline patterns at various Rayleigh number with two obstacles in the cavity. Their presence impedes the fluid flow and thus the constriction in the streamline patterns takes place as in Figs. 17(*a*)–17(*c*). Secondary vortices are generated near the obstacle and the flow becomes complex in nature as indicated in Fig. 17(*c*). Figure 17(*d*) delineates the streamline patterns at

$Ra = 10^6$. Figure 18 shows the isotherms obtained at various Rayleigh numbers for cavity with two obstacles. Antisymmetry of isotherm patterns for all Rayleigh numbers is observed.

Figure 19 depicts the streamline patterns for cavity in presence of four adiabatic obstacles. It is seen that one more recirculation zone is formed behind all the obstacles at $Ra = 10^6$.The intensity of the recirculation is higher for top left obstacle when compared to the top right obstacle. Similar is the case with the bottom obstacles. This occurs due to the initial development of flow from the bottom of the wall while ascending gains the higher momentum compared to the momentum at the bottom. Later, when the fluid reaches near the cold wall, the net buoyancy force gets reduced, thus decreasing the fluid flow. The rate of circulation depends largely on the buoyancy force and the friction of the walls. A similar phenomenon is seen to occur when the fluid descends along the cold wall. Figure 20 represents the isotherm contours at various Rayleigh numbers with four obstacles in the cavity.

Table 4 analyzes the Nusselt number variation with presence of number of obstacles. The heat transfer rate is found to be decreased with the increase in number of obstacles. The placement of adiabatic obstacles outside of conduction dominant zone does not improve the heat transfer rate.

4 Conclusion

In the present work, LBM is used to study the two-dimensional natural convection in a square enclosure with one, two, and four numbers of obstacles. First, the effect of single adiabatic obstacle in the cavity is discussed in terms of streamline patterns, isotherms, and Nusselt number. At various Rayleigh numbers, the optimum sizes of adiabatic obstacle are obtained. The optimum size for heat transfer enhancement for Rayleigh number $Ra = 10^4$, 10^5, and 10^6 is found to be 20%, 50%, and 60%, respectively, of the size of the cavity discussed in present study. However, at $Ra = 10^3$, the conduction is dominant and therefore the increment of Nusselt number could not be seen even at $\phi = 0.03$ of the size of the cavity. For $Ra = 10^3$ and 10^4, significant variation is observed in the hot wall Nusselt number with the variation of ϕ; however, for $Ra = 10^5$ and 10^6, little deviation or no deviation along hot wall Nusselt number is observed. The placement of obstacles outside the core zone of conduction could not lead to heat transfer enhancement rather the deterioration of heat transfer rate. The reduction of Nusselt number from no obstacle to four obstacles in a cavity is 21.32%, 40.72%, 16.51%, and 1.43%, for Rayleigh number $Ra = 10^3$, 10^4, 10^5, and 10^6, respectively.

Acknowledgment

Authors thank the Department of Mechanical Engineering, National Institute of Technology Karnataka, Surathkal, Mangalore, for providing support and facilities.

References

[1] Kruger, T., Kusumaatmaja, H., Kuzmin, A., Shardt, O., Silva, G., and Viggen, E. M., 2017, *The Lattice Boltzmann Method: Principles and Practice*, Springer International Publishing, Basel, Switzerland.

[2] Chen, S., and Doolen, G. D., 1998, "Lattice Boltzmann Method for Fluid Flows," Annu. Rev. Fluid Mech., **30**, pp. 282–300.

[3] Frisch, U., Hasslacher, B., and Pomeau, Y., 1986, "Lattice-Gas Automata for the Navier-Stokes Equations," Phys. Rev. Lett., **56**(14), pp. 1505–1508.

[4] Sthavishtha, B. R., Perumal, D. A., and Yadav, A. K., 2018, "Computation of Fluid Flow in Double Sided Cross-Shaped Lid-Driven Cavities Using Lattice Boltzmann Method," Eur. J. Mech.—B/Fluids, **70**, pp. 46–72.

[5] Succi, S., Santangelo, P., and Benzi, R., 1988, "High-Resolution Lattice-Gas Simulation of Two-Dimensional Turbulence," Phys. Rev. Lett., **60**(26), pp. 2738–2740.

[6] Martinez, D. O., Chen, S., and Matthaeus, W., 1994, "Lattice Boltzmann Magnetohydrodynamics," Phys. Rev. E, **47**(4), pp. R2249–R2252.

[7] Martys, N. S., and Chen, H., 1996, "Simulation of Multicomponent Fluids in Complex Three Dimensional Geometries by the Lattice Boltzmann Method," Phys. Rev. E, **53**(1), pp. 743–750.

[8] Martys, N. S., and Douglas, F. F., 2001, "Critical Properties and Phase Separation in Lattice Boltzmann Fluid Mixtures," Phys. Rev. E, **63**(3), p. 031205.

[9] Massaioli, F., Benzi, R., and Succi, S., 1993, "Exponential Tails in Two-Dimensional Rayleigh-Benard Convection," Europhys. Lett., **21**(3), pp. 305–310.

[10] Dixit, H. N., and Babu, V., 2006, "Simulation of High Rayleigh Number Natural Convection in a Square Cavity Using the Lattice Boltzmann Method," Int. J. Heat Mass Transfer, **49**(3–4), pp. 727–739.

[11] Braga, E. J., and de Lemos, M. J. S., 2005, "Heat Transfer in Cavities Having a Fixed Amount of Solid Material," ASME Paper No. HT2005-72719.

[12] Mousa, M. M., 2016, "Modeling of Laminar Buoyancy Convection in a Square Cavity Containing an Obstacle," Bull. Malaysian Math. Sci. Soc., **39**(2), pp. 483–498.

[13] Regulski, W., and Szumbarski, J., 2012, "Numerical Simulation of Confined Flows Past Obstacles—The Comparative Study of Lattice Boltzmann and Spectral Element Methods," Arch. Mech., **64**(4), pp. 423–456.

[14] Bhave, P., Narasimhan, A., and Rees, D. A. S., 2006, "Natural Convection Heat Transfer Enhancement Using Adiabatic Block: Optimal Block Size and Prandtl Number Effect," Int. J. Heat Mass Transfer, **49**(21–22), pp. 3807–3818.

[15] Merrikh, A. A., and Mohamad, A. A., 2001, "Blockage Effects in Natural Convection in Differentially Heated Enclosure," J. Enhanced Heat Transfer, **8**(1), pp. 55–72.

[16] House, J. M., Beckermann, C., and Smith, T. F., 1990, "Effect of a Centered Conducting Body on Natural Convection Heat Transfer in an Enclosure," Numer. Heat Transfer Part A, **18**(2), pp. 213–225.

[17] Xu, F., Patterson, J. C., and Lei, C., 2006, "Experimental Observations of the Thermal Flow Around a Square Obstruction on a Vertical Wall in a Differentially Heated Cavity," Exp. Fluids, **40**(3), pp. 364–371.

[18] Merrikh, A. A., Lage, J. L., and Mohamad, A. A., 2002, "Comparison Between Pore Level and Porous Medium Model for Natural Convection in a Nonhomogeneous Enclosure," *Fluid Flow and Transport in Porous Media: Mathematical and Numerical Treatment*, Z. Chen and R. E. Ewing, eds., American Mathematical Society, Providence, RI, pp. 387–396.

[19] David, E., and Lauriat, G., 1989, "Analogy Between Wall Channeling Effects in Porous Media and Thermal Convection Loops," Numer. Methods Therm. Probl., **6**, pp. 476–486.

[20] Roslan, R., Saleh, H., and Hashim, I., 2014, "Natural Convection in a Differentially Heated Square Enclosure With a Solid Polygon," Sci. World J., **2014**, p. 617492.

[21] Ha, M. Y., Kim, I.-K., and Yoon, H. S., 2002, "Two-Dimensional and Unsteady Natural Convection in a Horizontal Enclosure With a Square Body," Numer. Heat Transfer A: Appl., **41**(2), pp. 183–210.

[22] Hussain, S. H., and Hussein, A. K., 2011, "Mixed Convection Heat Transfer in a Differentially Heated Square Enclosure With a Conductive Rotating Circular Cylinder at Different Vertical Locations," Int. Commun. Heat Mass Transfer, **38**(2), pp. 263–274.

[23] De Vahl Davis, G., 1983, "Natural Convection of Air in a Square Cavity: A Benchmark Solution," Int. J. Numer. Methods Fluids, **3**(3), pp. 249–264.

[24] Mohamad, A. A., 2011, *Lattice Boltzmann Method, Fundamentals and Engineering Applications With Computer Codes*, Springer, London.